Ecole MATMECA

MATMECA
Ecole d'Ingénieurs en Modélisation Mathématique et Mécanique

National Institute of Water and Atmospheric Research

NIWA
Taihoro Nukurangi

HYDRODYNAMIC TIDAL MODEL OF COOK STRAIT

Rym Msadek   Promotion 2005

Supervisor: Stéphane Popinet
Academic Supervisor: Mejdi Azaiez

Abstract

Ocean straits are regions of enhanced dynamic activity characterised by large mixing of water masses. Therefore, they stand as challenging places to make model prediction.

We investigate the tidal response of coastal waters in Cook Strait, separating the North Island from the South Island in New Zealand. The simulations are run using the *Gerris* Flow Solver. The model implemented is based on the linearized 2-dimensional shallow water equations. The open boundaries are forced with the M2 tidal constituent, extracted from a high resolution larger-scale encompassing model.

In this report, the distributions of amplitude and current are described in details. Validation of the numerical model is achieved by comparing with the global scale model data and with sea level and current measurements. The sea level amplitude and phase turned out to be in very good agreement with those obtained from the driving model and observations. The results obtained for the distribution of current were also satisfactory despite the lack of observed data in the geographical area of interest.

Contents

List of Tables

List of Figures

1 Introduction

New Zealand is in the Southern Hemisphere, lying on the South-West of the Pacific Ocean, and is comprised of two major islands.

Accurate knowledge of ocean dynamics and particularly tides propagation is critical for predicting shoreline change and pollutant transport on coastal regions, with applications in oil spill and dredging operations management.

Significant progress has been made in the development of numerical models for ocean circulation in this region. Actually, Bye & Heath [2], Heath [8], and LeProvost et al. [3] exhibited the complete rotation of the semi-diurnal tides around New Zealand. It means that at any given time we can observe both high and low tide somewhere along the New Zealand Coast. Recently, Walters et al. [14] developed a barotropic model in the area within New Zealand's Exclusive Economic Zone, driven by TOPEX/Poseidon altimeter data on the outer ocean boundaries. Their results were compared with those from field observations and good agreements were obtained.

In the work presented here we will focus on the area around Cook Strait illustrated in Fig 1. A strait is a narrow channel that separates two larger bodies of water, and thus lies between two land masses. Cook Strait connects Northern and Southern Islands in New Zealand and it is 24 kilometres wide at its narrowest point. This area is of special scientific interest mainly because its topography gives rise to worthwhile dynamics.

The *Gerris Flow Solver* is run to simulate oceanic circulation in Cook Strait. The model implemented in *Gerris* is based on the linearized 2-dimensional shallow water equations. The tide is introduced along the open boundary using the larger-scale encompassing model data.

The goal of this project is to obtain accurate amplitudes and phases for sea-level and to examine the distribution of current in order to provide a validation of the oceanic numerical model. To accomplish this, we will compare the predicted tidal results with observations and with the global ocean model developed by Walters et. al [14], which has been validated.

After explanations about the theory of tides, we will first give a description of the model underlining the importance of boundary conditions. Then we will present the results and discuss their accuracy.
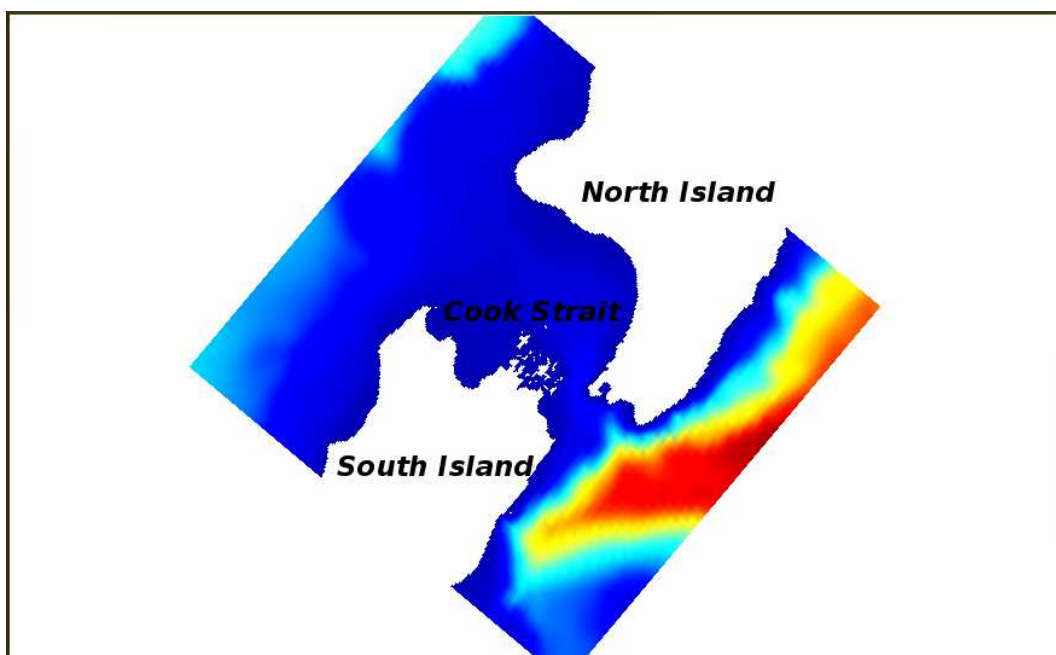
Figure 1: Bathymetry around Cook Strait.

2 Origin of tides

2.1 A simple model: the equilibrium theory

Tides are the result of gravitational attraction between stellar bodies, mainly the Moon and Sun. The simplest concept of tides, called the equilibrium theory was first proposed by Newton in 1687. In this model, we assume that the Earth is not rotating and that it is fully covered by water. Then the tide-raising forces at the Earth's surface result from a combination of two basic forces: the force of gravitation exerted by the Moon (and Sun) upon the Earth, and the centrifugal force produced by the revolutions of the Earth and Moon (and Earth and Sun) around their common centre-of-gravity. Then if one considers the Moon-Earth system, there is a balance between the gravitational attraction and the centrifugal acceleration of both with respect to a common axis of rotation. However, although the centrifugal force is the same for all points on the Earth, there are slight differences in the gravitational attraction. In fact, the force of gravity is proportional to the product of the masses of the two objects and inversely proportional to the square of the distance between them. Therefore the gravitational force is larger at points on the Earth's surface closer to the Moon and smaller at points on the opposite side. The residual force acting towards or away from the Moon is called the lunar tide-generating force. Since the Earth is assumed to be completely covered by oceans and because water particles are free to move, the tidal deformation produces two tidal bulges.

The situation is illustrated schematically in Fig.2. Here we have displayed the combination of forces of lunar origin producing the tides. F_c refers to the centrifugal force due to the Earth's revolution around the barycenter, F_g represents the gravitational attraction of the Moon, and the resultant tide-generating force is called F_t.
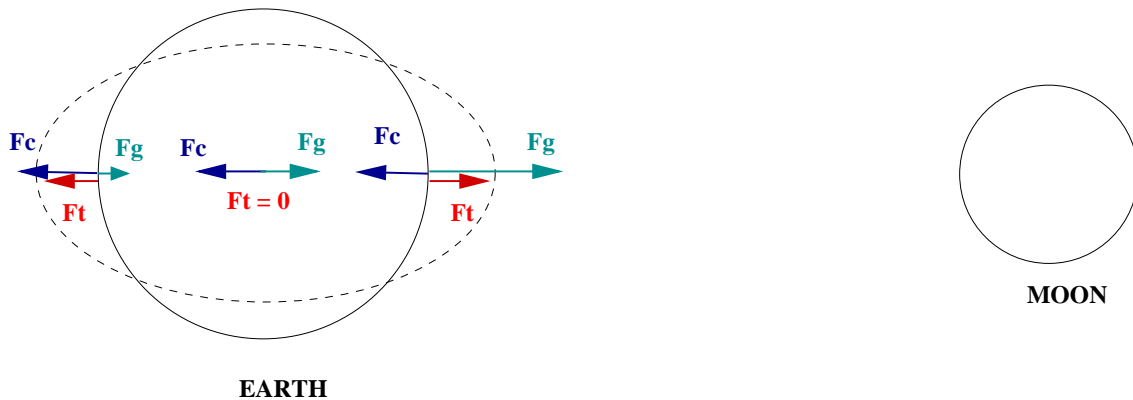
Figure 2: Tidal bulges.

The same applies for the Sun-Earth system, but the solar tide-generating force is only about three-sevenths of the lunar on account of the greater distance of the Sun from the Earth.

Although the tide-generating force is very weak compared to the Earth's gravitational force, it is a body force, which means that it acts on all the mass of the fluid and besides it acts horizontally, hence the resulting significant effects.

2.2 The dynamic theory of tides

However, even if the equilibrium theory easily describes the well-known tidal phenomena, it appears to be inexact. Actually, the predicted rises are too small compared to the observed tides, thus this theory does not give a good description of ocean motions mainly because it does not take into account the existence of continents and the fact that ocean basins have irregular shapes. Then in contrast to the static theory, the dynamic theory of tides recognises that the Earth is rotating and that only three-quarters of our planet are covered by water. In this theory proposed by Laplace in 1775, tides are viewed as forced waves driven by the periodic fluctuation of the tidal forces. They act as shallow water waves, i.e, they continually interact with the bottom.

2.3 Harmonic motion and tidal constituents

As we described them above, tides are considered as waves driven by the periodic oscillations of the tidal forces. Every finite volume of fluid has its own preferred wave frequencies, then if there is a periodic motion, the reaction of the fluid will be much stronger if the forcing occurs at one of these resonance frequencies than if

it occurs at other frequencies. Taking into account the size of a water body, we can calculate the resonance frequencies of specific basins, and then determine the amplitude and phase of the tidal wave generated. Only the largest water bodies such as the major oceans can experience tidal forcing because marginal seas cannot produce a response to astronomical tide forcing. Then the tide-producing force generates forced waves in the ocean and the rise and fall called tide is simply a result of the flow convergence or divergence there. As the position and movement of the Sun and Moon are known in great detail, the tidal forces can be determined precisely. The tide-generating force of either body is greater the nearer the body is to the Earth.

Moreover, a tide is the resultant of a number of constituents, each of which is a simple harmonic motion. According to the period of these constituents, a tide can be diurnal (one cycle a day), semi-diurnal (two cycles a day), or long period. Each constituent is defined by its speed, the increment in phase in degrees per hour, and its amplitude. Almost all the constituents have been named. They are divided into semi-diurnal tides with a period of about half a day ($M_2, S_2, N_2, K_2,$), and diurnal tides with a period of about a day (O_1, K_1, P_1, Q_1). They are referenced in Table 5, Appendix A.

The Earth is in direct line with the Moon once every lunar day, which is on average about 24 hours 50 minutes. Then the interval between successive high waters caused by the lunar-tide generating force is on average 12 hours 25 minutes.

The tides around New Zealand are predominantly semi-diurnal and the dominant component is the M_2 tidal constituent. Thus there are usually two high tides and two low tides which come about 50 minutes later each day.

Tidal streams are a direct effect of tides, but whereas the tides are periodic vertical movements of the water, tidal streams are periodic horizontal movements. Tidal currents play a significant role in the ocean circulation. They are predominantly parallel to the shore and tend to be more important as the water depth decreases.

3 Tidal model

3.1 The *Gerris* Flow Solver

The *Gerris* Flow Solver is an open source code developed since 2001 by Dr. Stéphane Popinet. The source code is freely available at *http://gfs.sourceforge.net*.

Gerris solves the incompressible Navier-Stokes equations, or the 2-dimensional shallow water and 3-dimensional hydrostatic oceanic equations. The pressure is calculated using a Multigrid Poisson Solver for Navier-Stokes equations, and the oceanic equations are solved using a semi-implicit multigrid barotropic solver. The specificity of *Gerris* is its adaptative mesh refinement: the resolution is adapted spatially and dynamically. Then it can take into account the complexity of topography, and depending on the features of the flow it will also focus mainly on the regions where refinement is useful. This allows to save computing time. Significant improvement has been made in the code since its creation and it is still being actively worked on.

Gerris is a console-based program. It takes a parameter or simulation file as input and produces various types of files as output. Everything needed to run the simulation is specified in the parameter file, including:

- layout of the simulation domain,

- initial conditions,

- boundary conditions,

- solid boundaries,

- what to output (and when),

- control parameters for the numerical schemes.

The output solution is viewed using *GfsView*, a stand-alone application for visualising *Gerris* simulation files, developed by S. Popinet. In contrast to former options (Geomview, OpenDX, Mayavi), it makes full use of the octree representation to efficiently process and display simulation files. In this project we attempt to improve the tidal model by finding the appropriate boundary conditions.

The region of interest shown on Fig. 1, is 500 kilometres wide. The domain is spatially discretized using square finite volumes. At the beginning of the simulation the domain is a square. We can divide this initial square into 4 others, and we keep splitting each square until the required refinement is reached. Then this discretization can be represented as a quadtree. Fig. 3 shows the quadtree-based grid of the domain, and Fig.4 gives the corresponding tree representation.

The mesh is spatially refined near coastal boundaries to take into account the complexity of topography. Thus the minimum cell size is 0.97 km near land, and the maximum cell size is 7.8 km within the rest of the domain.
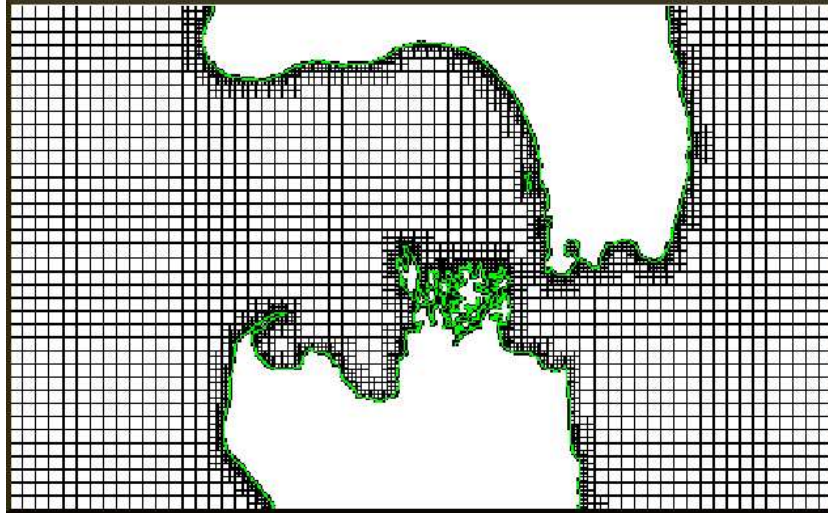
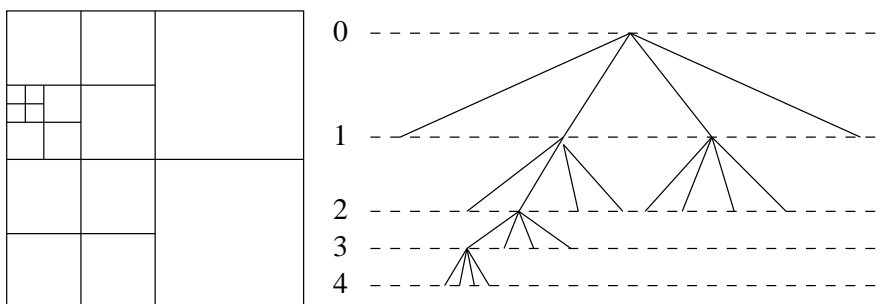Figure 3: Quadtree-based grid of Cook Strait.

Figure 4: Example of quadtree discretization and corresponding tree representation.

3.2 Shallow water theory

The numerical model implemented in *Gerris* is based on the linearized 2-dimensional shallow water equations, where the hydrostatic approximation is used as detailed in [12].

We consider a sheet of fluid with a constant and uniform density. The height of the surface of the fluid above the reference level $z = 0$ is $h(x, y, t)$. The rigid bottom is defined by the surface $z = h_B(x, y)$ so that the total depth is defined by $H = h - h_B$. The velocity has components u, v parallel to the x-, y- axes respectively. The equations of mass conservation and horizontal momentum are

$$\frac{\partial u}{\partial t} + u \frac{\partial u}{\partial x} + v \frac{\partial u}{\partial y} - fv + k \frac{u}{H} = -g \frac{\partial h}{\partial x}, \tag{1}$$

$$\frac{\partial v}{\partial t} + u \frac{\partial v}{\partial x} + v \frac{\partial v}{\partial y} + fu + k \frac{v}{H} = -g \frac{\partial h}{\partial y}, \tag{2}$$

$$\frac{\partial H}{\partial t} + \frac{\partial}{\partial x} \left(uH \right) + \frac{\partial}{\partial y} \left(vH \right) = 0, \tag{3}$$

where g is the acceleration of the Earth's gravity, k is the coefficient of bottom friction, $f = 2\Omega \sin \Phi$, with Ω the angular velocity of the earth, and Φ the geographic latitude. Consequently, the terms fv and fu in eq. (1) and (2) refer to the horizontal component of the Coriolis force.

We define H_0, the depth in absence of motion. Then

$$H(x, y, t) = H_0(x, y) + \eta(x, y, t), \tag{4}$$

where η represents the elevation of the sea surface. We assume the amplitude of motion to be small which implies

$$\eta \ll H_0. \tag{5}$$

Moreover u and v are supposed to be small enough that the advective terms can be ignored as follows

$$\frac{\partial \mathbf{u}_H}{\partial t} \gg \mathbf{u}_H . \nabla \mathbf{u}_H, \tag{6}$$

where $\mathbf{u}_H$ is the horizontal velocity defined by

$$\mathbf{u}_H = \mathbf{i} u + \mathbf{j} v. \tag{7}$$

Then the linearized shallow water equations are

$$\frac{\partial u}{\partial t} - fv + k \frac{u}{H_0} = -g \frac{\partial \eta}{\partial x}, \tag{8}$$

$$\frac{\partial v}{\partial t} + fu + k \frac{v}{H_0} = -g \frac{\partial \eta}{\partial y}, \tag{9}$$

$$\frac{\partial \eta}{\partial t} + \frac{\partial}{\partial x} \left(uH_0 \right) + \frac{\partial}{\partial y} \left(vH_0 \right) = 0. \tag{10}$$

We define the mass flux vector components by

$$U = uH_0, \tag{11}$$

$$V = vH_0. \tag{12}$$

Then (8), (9) and (10) become

$$\frac{\partial U}{\partial t} - fV + k \frac{U}{H_0} = -gH_0 \frac{\partial \eta}{\partial x}, \tag{13}$$

$$\frac{\partial V}{\partial t} + fU + k \frac{V}{H_0} = -gH_0 \frac{\partial \eta}{\partial y}, \tag{14}$$

$$\frac{\partial \eta}{\partial t} + \frac{\partial U}{\partial x} + \frac{\partial V}{\partial y} = 0. \tag{15}$$

3.3 Spectral analysis

We can express the dependent variables U, V and η as an harmonic expansion of the main tidal constituents represented by cosine functions. The purpose of tide analysis is to determine the amplitude and phase of the cosine waves. Our analysis will only include the principal lunar semi-diurnal constituent M_2. Then the tide is represented by the following equation

$$\eta(t) = R_0 \cos(w_0 t - \phi), \tag{16}$$

where $\eta(t)$ is the height of the tide at time t, R_0 is the amplitude (equal to one-half the tidal range), ϕ is the phase in degrees, and $w_0 = 28.984$ degrees per mean solar hour, is the speed. We are interested in finding the best approximation f to a function consisting of one particular frequency $f_0 = w_0/2\pi$ known, and we are seeking the correspondent amplitude. This will be solved using the method of least squares. We wish to find the best fit curve using the function

$$f(t) = Z + A_0 \cos(w_0 t) + B_0 \sin(w_0 t), \tag{17}$$

where Z, A_0 and B_0 are the unknown parameters. Then we deduce the amplitude and phase by writing

$$R_0 = \sqrt{A_0^2 + B_0^2}, \tag{18}$$

$$\phi = \arctan\left(\frac{B_0}{A_0}\right). \tag{19}$$

3.4 Initial conditions

Because of the frictional dissipation, the influence of initial conditions becomes insignificant after some time. Therefore co-oscillating tides may be generated from any specified initial state given by

$$\eta, u, v\, (x, y, t) \qquad \text{at} \qquad t = 0. \tag{20}$$

In this model the initial state is generated using a *GTS* triangulated surface. *GTS* is an open source free software also developed by Dr. Stéphane Popinet and available at *http://gts.sourceforge.net/*. Among its main features, it allows to deal with constrained Delaunay triangulations.

3.5 Boundary conditions

3.5.1 Coastal boundary condition

The land boundary is rigid and impermeable to fluid motion which is expressed in the numerical model by a zero normal flow given by

$$\mathbf{u}_H.\mathbf{n} = 0, \tag{21}$$

where $\mathbf{u}_H$ is the horizontal velocity defined in (7), and $\mathbf{n}$ is the outward unit normal vector.

3.5.2 Open boundary conditions

According to Roed and Cooper [13]

> "an open boundary is a computational boundary at which disturbances originating at the interior of the computational domain are allowed to leave it without disturbing or deteriorating the interior solution."

The construction of open boundary conditions has been a subject of conjecture over the last 40 years and a large number of open boundary conditions have been proposed in the literature (see [11] and [4] for a recent review). Nycander and Döös [9] and P. Marchesiello et al. [10] have tested several open boundary conditions for barotropic waves on the one hand, and for oceanic models on the other hand. Results from these studies indicate that the Flather condition [5] seems particularly suited to the treatment of tidal waves. Moreover Blayo and Debreu [4] emphasized the well-posedness of the model equations using these open boundary conditions. First, the tide is introduced along the open sea boundary by specifying elevation as a function of position and time

$$\eta = \hat{\eta}\,(x, y, t) = R \cos(wt - \phi). \tag{22}$$

where R is the amplitude of sea level and ϕ is the phase. The input data $\hat{\eta}$ can be extracted from observations (*in-situ* measurements), or published cotidal charts or eventually from larger encompassing models. Flather and Heaps [6] showed that a global scale model offers the best input data.

The model presented here is forced at the boundaries with Walters et al. data [14] resulting from a high-resolution model encompassing New Zealand's Exclusive Economic Zone and driven at the open ocean boundaries by TOPEX/Poseidon (T/P) altimeter data.

Here, tidal forcing is introduced into the model by extracting the semi-diurnal constituent M_2 from the encompassing model. We investigate the best boundary condition so that the solution within the domain will be as close as possible to the feature of the larger scale model.

Actually the condition specified in (22) is found in some cases to not adequately model physical behaviour as it will be detailed in section 3.6. Therefore we investigate a condition which uses both sea level forcing and barotropic transport to reproduce realistically the tidal wave. A radiation condition applied to the velocity at the boundary was described by Flather [5]. It requires a specification of both elevation ($\hat{\eta}$) and normal velocity ($\hat{u}_n$) at the boundary, related by

$$u_n = \hat{u}_n(x, y, t) + \frac{c}{H_0}[\eta - \hat{\eta}(x, y, t)], \tag{23}$$

where $c = \sqrt{gH_0}$.

Practically, this condition is computed using an iterative scheme. First we take $\hat{u}_n = 0$ and the prescribed $\hat{\eta}$ using (23). The first computation yields $u_n = u_n^{(1)}$ and $\eta = \eta^{(1)}$ on the open boundary. Then we run another simulation and we substitute $u_n = u_n^{(1)}$ in (23) and we reiterate the calculation to obtain $u_n = u_n^{(2)}$ and $\eta = \eta^{(2)}$. We keep repeating this procedure until we notice there is no significant change in either u_n or η on the open boundary from one tidal solution to the next. The final solution then obtained is the correct one since in it $\eta = \hat{\eta}$ on the open boundary as required. The rapidity of convergence depends on the location of the boundary point.

Solution	$\hat{u}$		$\hat{v}$		$\hat{\eta}$		u		v		η	
	M_u (cm/s)	ϕ (deg)	M_u (cm/s)	ϕ (deg)	M_u (cm)	ϕ (deg)	M_u (cm/s)	ϕ (deg)	M_u (cm/s)	ϕ (deg)	M_u (cm)	ϕ (deg)
1	0.0	−	0.0	−	117.3	−63.9	3.1	−80.0	6.2	106.8	109.5	−53.1
2	3.1	−80.0	6.2	106.8	"	"	2.9	−85.4	6.3	123.8	117.2	−62.3
3	2.9	−85.4	6.3	123.8	"	"	2.8	−78.8	5.4	128.3	115.4	−63.5
4	2.8	−78.8	5.4	128.3	"	"	3.0	−75.6	4.7	123.1	115.4	−63.5
5	3.0	−75.7	4.7	123.1	"	"	3.0	−73.7	4.6	116.3	115.9	−63.5
6	3.0	−73.7	4.6	116.3	"	"	3.0	−71.8	4.7	111.8	116.3	−63.6
7	3.0	−71.8	4.7	111.8	"	"	3.0	−70.7	4.8	109.1	116.7	−63.6
8	3.0	−70.6	4.8	109.1	"	"	2.9	−70.5	5.0	107.5	116.9	−63.6
9	2.9	−70.5	5.0	107.5	"	"	2.8	−71.1	5.1	106.7	117.1	−63.5
10	2.8	−71.0	5.1	106.7	117.3	−63.9	2.8	−72.4	5.1	106.3	117.1	−63.5

Table 1: Iterative procedure on a boundary point near New Plymouth.

Solution	$\hat{u}$		$\hat{v}$		$\hat{\eta}$		u		v		η	
	M_u (cm/s)	ϕ (deg)	M_u (cm/s)	ϕ (deg)	M_u (cm)	ϕ (deg)	M_u (cm/s)	ϕ (deg)	M_u (cm/s)	ϕ (deg)	M_u (cm)	ϕ (deg)
1	0.0	−	0.0	−	115.2	−52.9	3.9	−139.8	5.4	115.2	114.4	−44.2
2	3.8	−140.7	5.4	115.4	"	"	4.1	−142.5	7.9	125.9	116.6	−51.9
3	4.1	−142.5	7.9	125.9	"	"	4.1	−139.2	8.6	126.9	113.2	−53.2
4	4.1	−139.2	8.6	126.9	"	"	4.1	−135.7	9.1	126.3	113.4	−53.5
5	4.1	−135.8	9.1	126.4	"	"	4.1	−132.7	9.7	126.4	114.3	−53.7
6	4.1	−132.7	9.7	126.4	"	"	4.1	−130.2	10.1	127.0	115.0	−53.7
7	4.1	−130.3	10.1	127.0	"	"	4.0	−128.2	10.4	128.0	115.6	−53.7
8	4.0	−128.2	10.4	128.0	"	"	4.0	−126.5	10.6	128.9	116.0	−53.6
9	4.0	−126.5	10.6	128.9	"	"	4.0	−125.3	10.7	129.7	116.4	−53.5
10	3.9	−125.3	10.7	129.7	115.2	−52.9	3.9	−124.2	10.7	130.4	116.6	−53.4

Table 2: Iterative procedure on a boundary point north Charleston.

In Tables 1 and 2 we show two numerical examples that illustrate the procedure. We notice that the convergence is less rapid for the point north Charleston (Table 2) than near New Plymouth (Table 1). We approximately need 10 iterations to reach the final solution.

The horizontal velocity is split into u and v components whose amplitudes are M_u and M_v respectively, corresponding to the projection of the velocity vector on the local frame. In fact, New Zealand is located at 40º S, but the simulations ran on *Gerris* do not take into consideration this latitude. Therefore, to obtain the east-going

and north-going components of velocity we will have to convert the u and v components by taking into consideration the rotation of $-40°$.
The solution then obtained after these 10 iterations is the final solution we will use to analyse the results. The model predictions will be compared both with data resulting from the larger-scale model and with measurements. The observation data were courtesy of Walters et al.[14] and other NIWA staff members (M. Wild from NIWA Christchurch and M. Greig from NIWA Wellington).

3.6   Comparison between different open boundary conditions

In this section, results for the semi-diurnal tidal constituent M_2 are presented and compared with the driving model solution. We analyse the results for both open boundary conditions within the simulation domain. The inputs of each model are summarised on table 3.

	Model A: non-iterative	Model B: iterative
input	$\eta = \hat{\eta}\,(x,y,t)$ $= R\cos(wt - \phi)$	$u_n = \hat{u}_n\,(x,y,t) + \frac{c}{H_0}\,[\eta - \hat{\eta}\,(x,y,t)]$

Table 3: Classification of the open boundary conditions.

First the tide is introduced along the open sea boundary by specifying elevation (Model A). The amplitude and phase obtained for sea level and current are then compared with those corresponding to the global scale model. In that purpose, we examine the statistical differences between the encompassing model and the predicted data. The distribution of normalized differences are shown in Fig.5-6-7 and 8. The differences calculated were Walters et al. minus *Gerris* value.
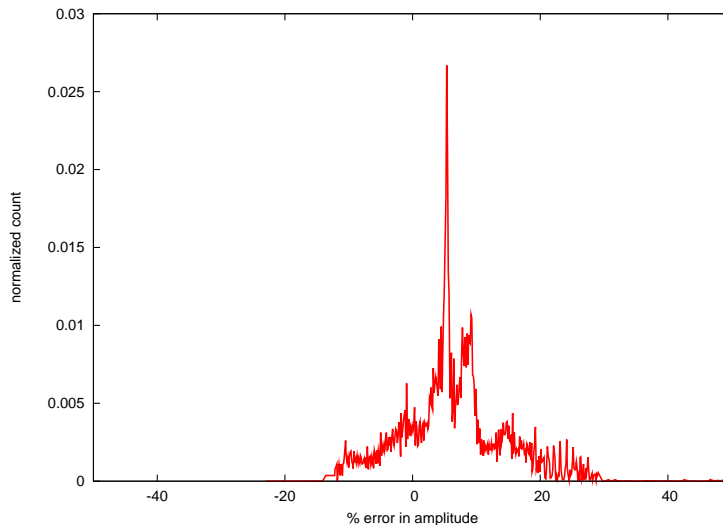

Figure 5: Distribution of normalized amplitude ratio for the M_2 tidal elevation, comparing the encompassing model with the results predicted by Model A.

From Fig .5 and 6, typical errors for elevation predicted using Model A, are the order of 20 % in amplitude and $10°$ in phase. The asymmetry in the distribution of errors also suggests a tendency to underestimate amplitudes and to overestimate phases.
Next, we analyse the tidal currents predicted by Model A. Fig.7 and 8 quantify the error for the amplitude of u and v velocity components respectively. We notice that the typical differences are under 0.5 m/s for both components and that u velocity component tends to be overestimated. This agreement is quite satisfactory. However, the accuracy of the amplitude elevation is not sufficient yet to validate our numerical model. Therefore we investigate another boundary condition that will take into consideration both tidal elevation and current.
As a result, a radiation condition (Model B) which requires a specification of both elevation and velocity, is applied at the boundary, as described in (23). The elevation errors are then quantified in Fig.9 and 10 which show the significant improvement using this iterative condition.
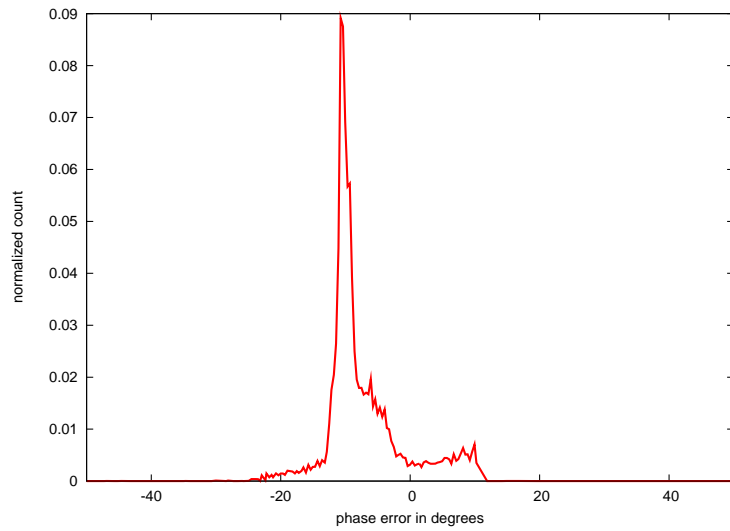
Figure 6: Distribution of phase difference between the encompassing model and Model A, for the M_2 tidal elevation.
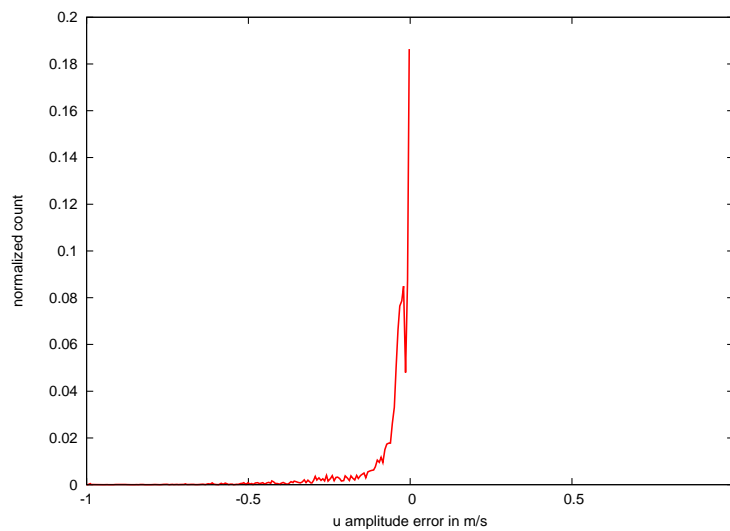

Figure 7: Distribution of amplitude difference of the u-velocity component, between the encompassing model and Model A, for the M_2 tidal constituent.
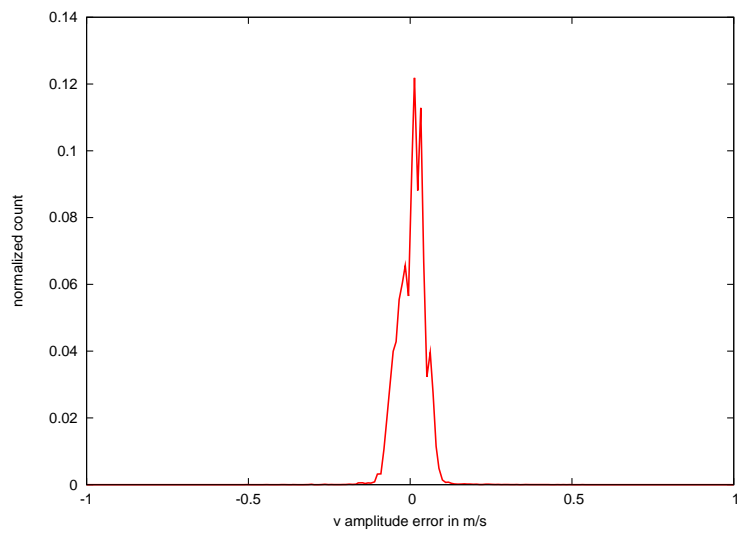
Figure 8: Distribution of amplitude difference of the v-velocity component, between the encompassing model and Model A, for the M_2 tidal constituent.
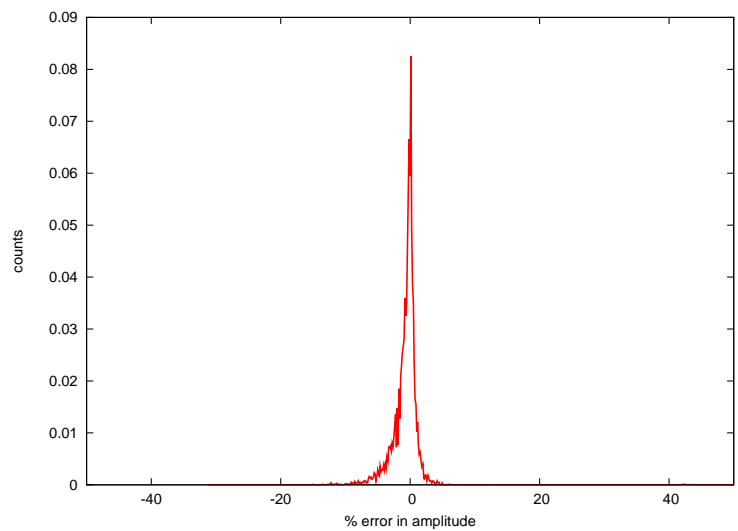

Figure 9: Distribution of normalized amplitude ratio for the M_2 tidal elevation, comparing the encompassing model with the results predicted by Model B.
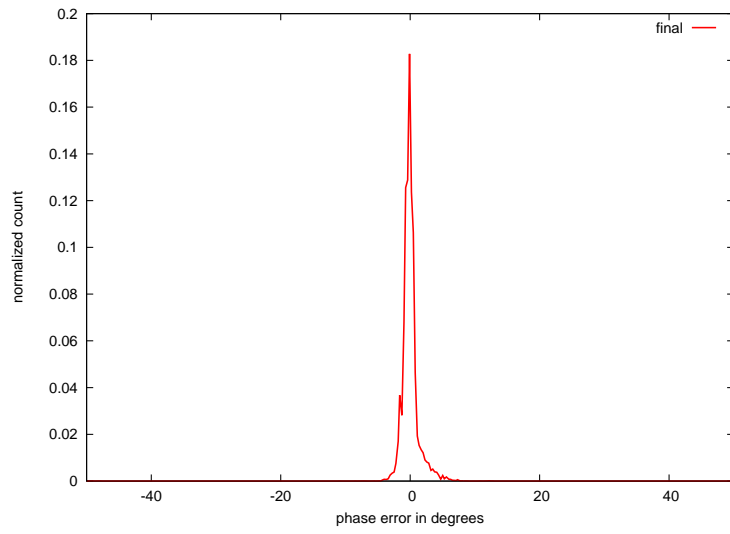
Figure 10: Distribution of phase difference between the encompassing model and Model B, for the M_2 tidal elevation.
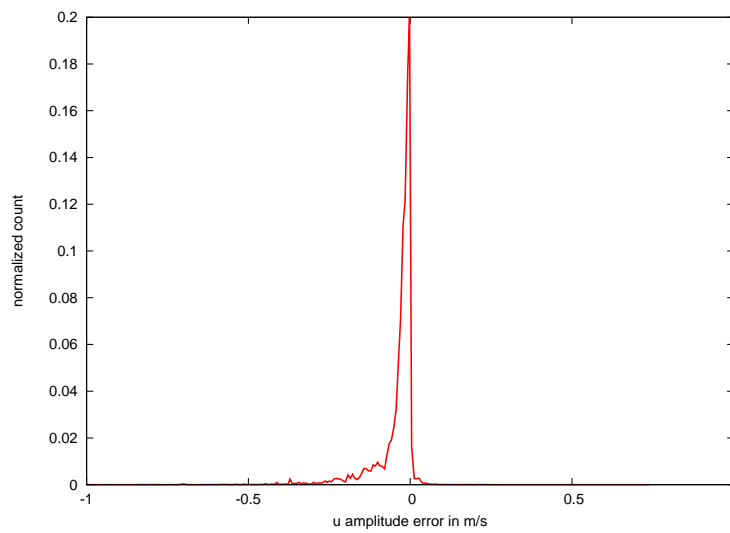

Figure 11: Distribution of amplitude difference of the u-velocity component, between the encompassing model and Model B, for the M_2 tidal constituent.
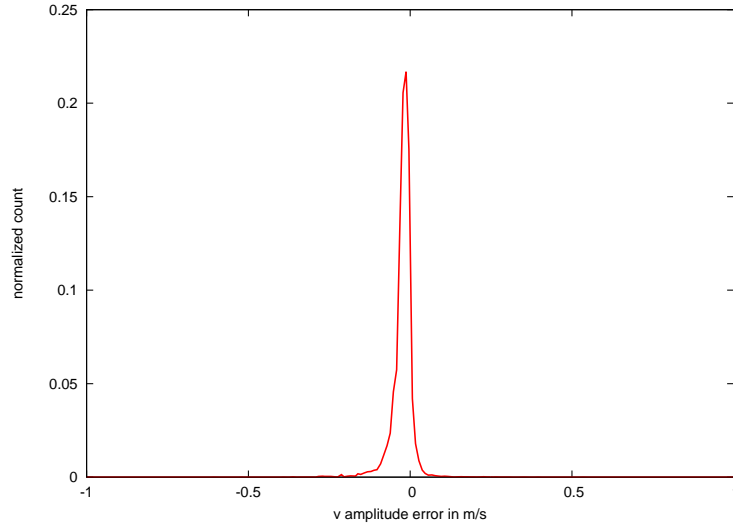
Figure 12: Distribution of amplitude difference of the v-velocity component, between the encompassing model and Model B, for the M_2 tidal constituent.

In fact the typical elevation error predicted by Model B is under 10 % in amplitude and under 5° in phase. Moreover the asymmetry is largely reduced. Besides, while using an iterative condition, the distribution of current is more in concordance with the larger-scale model. The corresponding difference for current is given in Fig.11 and 12. The changes concerning the distribution of current are not as important as the elevation ones. Nevertheless, we notice an improvement concerning the asymmetry of u velocity component and smaller errors are found concerning the amplitude of v velocity component.

Hence, while using an iterative condition, both tidal elevation and distribution of current are more in concordance with the larger-scale model. Appendix B provides the distribution of elevation errors at each step of the convergence. The difference tends to be smaller from one iteration to the next. Eventually, there is a significant improvement using the iterative procedure. Thus from now, we consider the iterative radiation condition to provide the best input along the outer boundary. Next, the tidal results will be presented for this solution.

3.7   The Sea surface elevation

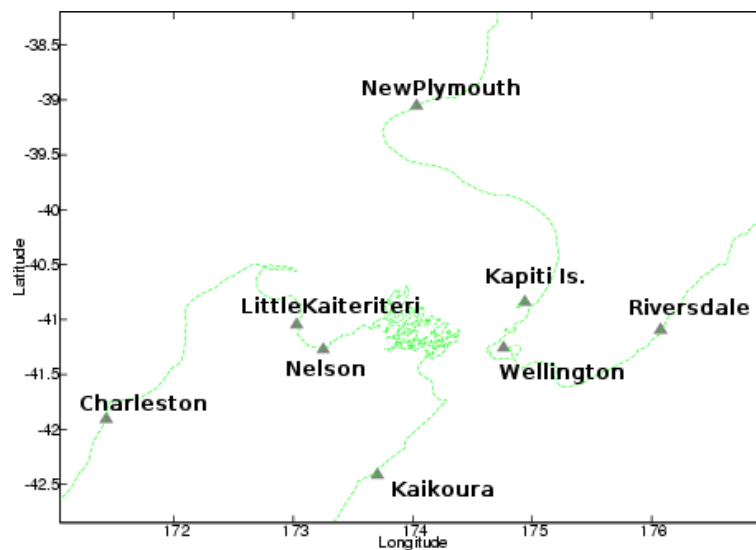Fig.13 displays the location of coastal cities we will next focus on.

Figure 13: Coastal sites of sea level analysis.

12

The results for the M2 tidal elevation are presented in Fig.14 and 16. In Fig.14, tidal amplitude is shaded using the scale of decreasing colours corresponding to descending values from 1.37 m for the red parts, to 0 m for the blue areas. We have displayed the M_2 tidal elevation of the driving model on the left and the corresponding solution obtained with *Gerris*, on the right. We notice the very good agreement with the driving model. In fact, the physical pattern of tides is well reproduced with a strong amplification along the west coast and near the land. Then the typical elevation on the west coast is above 1 m while it is under 0.7 m along the east coast. The maximum amplitude of 1.37 m is measured in Tasman Bay, near Nelson. The lowest values are registered in Cook Strait near Wellington.

Fig 15 provide an estimation of the error between the driving model and *Gerris*. The discrepancies become more important when we go closer to the coast in very shallow water. However, the maximum difference given by the infinity-norm is 10 cm and the averaged difference given by the 2-norm is only 2.5 cm which confirms the accuracy of *Gerris* model.
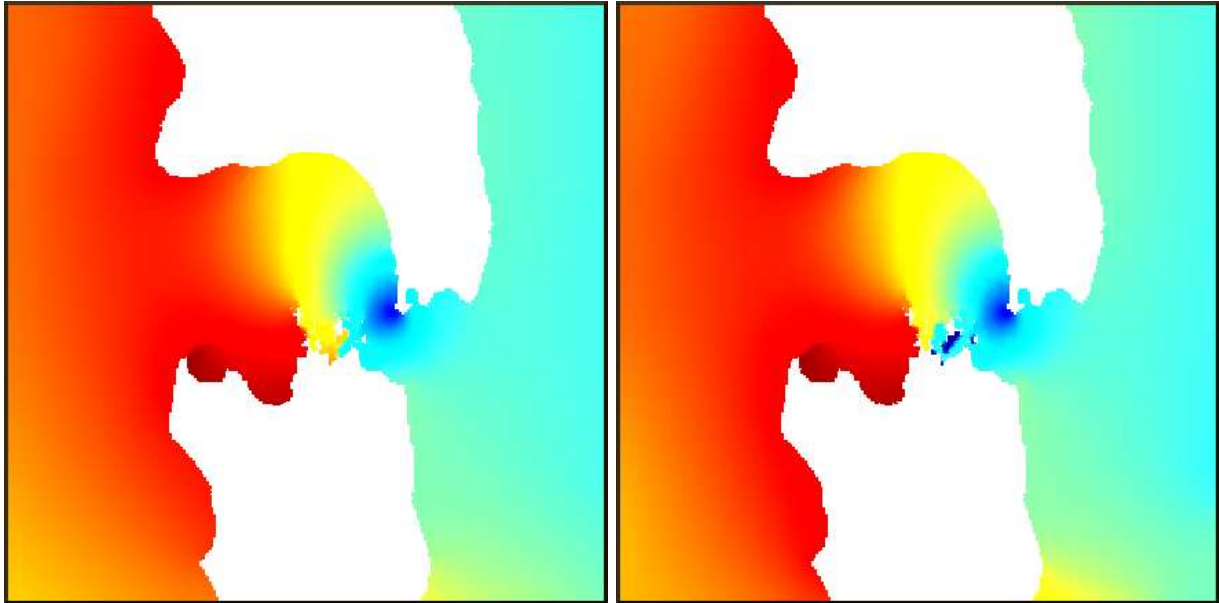

Figure 14: Comparison of M_2 amplitude elevation between the driving model (on the left) and *Gerris* (on the right). Amplitude is shaded using decreasing colours : min = 0 cm   max = 137 cm.
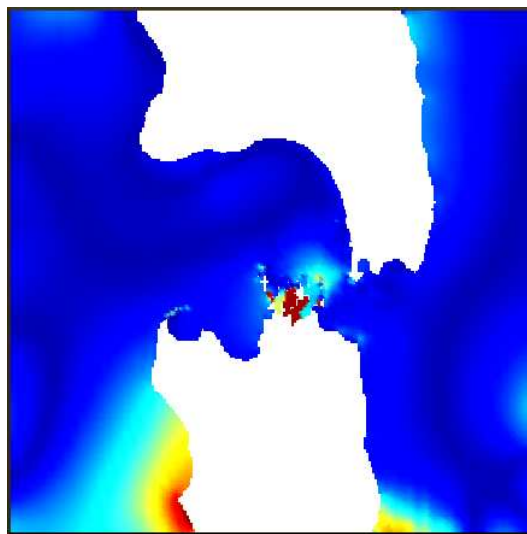

Figure 15: Amplitude error between *Gerris* model and the driving model. Error is shaded using decreasing colours : min = 0 cm   max = 10 cm.

The results for elevation phase are presented in Fig.16. Tidal phase is shaded using the scale of decreasing

colours corresponding to descending values from 360° for the red parts, to 0° for the blue areas. The results of the driving model are shown on the left and the solution obtained with *Gerris* is displayed on the right. We notice the very good agreement with the driving model. The M_2 tidal phase fluctuates between 0° on the west coast and 360° on the east, which means that at any given time there is always a high tide and a low tide somewhere along New Zealand coast. Therefore the phase difference across Cook Strait is quite significant and is the origin of the dynamics that occur like the strong currents.

Fig 17 provides an estimation of the phase difference between the driving model and *Gerris*. The error is more important in Cook Strait and near the sounds where the topography is complex. Then the maximum difference for the well resolved areas is 10°, and the averaged difference given by the 2-norm is only 3.1° which confirms the good agreement.
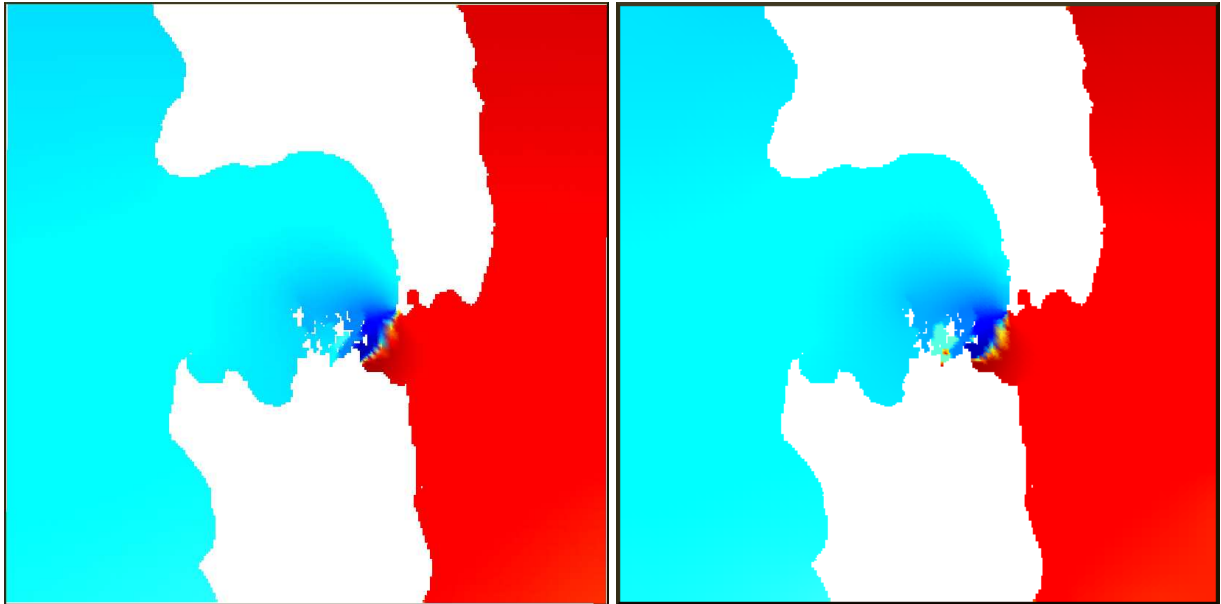

Figure 16: Comparison of M_2 phase elevation between the driving model (on the left) and Gerris (on the right). Phase is shaded using decreasing colours: min = 0°   max = 360°.
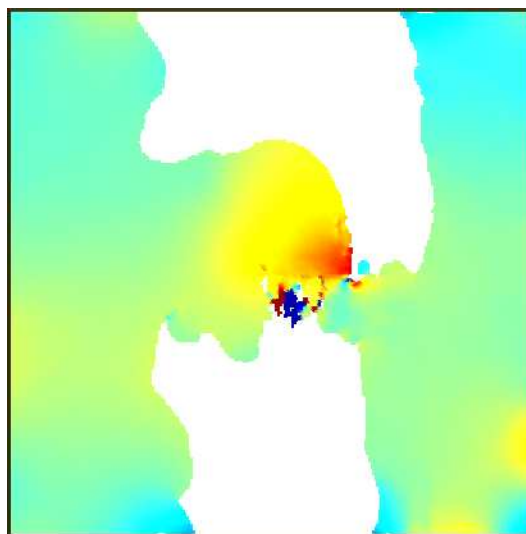

Figure 17: Phase difference between *Gerris* model and the driving model. Error is shaded using decreasing colours : min = −10°   max = 10°.

There is an area where the amplitude looks very low and when the phase lines converge. This part is

enlarged on Fig.18. The node near Wellington, in the south end of the North Island, coloured in deep blue and where the phase isolines meet, is an amphidromic point. An amphidromic point is a point within a tidal system where the tidal range is almost zero. It can be seen as the 2D equivalent of nodes in a standing wave pattern. Usually, these particular points occur because of a resonance phenomenon within an oceanic basin, generating a standing wave pattern which rotates around the nodal point. This stationary wave is a result of interference between two waves travelling in opposite directions. Then the distribution of current is formed by the superposition of these two waves propagating in opposite directions. Here the amphidrome is particular because it is located on land, then it is called a virtual (or degenerated) amphidrome. It is a different in that it is due to forced waves at each end of Cook Strait. Around New Zealand, the semi-diurnal tides are viewed as trapped Kelvin waves which are coastal gravity driven waves that balance the Earth's Coriolis force in the ocean. Kelvin waves are non-dispersive, i.e., the phase speed of the wave crests is equal to the group speed of the wave energy for all frequencies. Usually, Kelvin waves propagate around the northern (respectively southern) hemisphere oceans in a counterclockwise (respectively clockwise) direction using the coastline as a wave guide. The situation around New Zealand is quite unusual. Commonly in the Southern hemisphere the tides rotate around an amphidromic point in a cyclonic sense (i.e., clockwise) whereas around New Zealand the cotidal lines rotation around the node is anticyclonic. This feature was outlined by Heath [8]. Moreover, Egbert et al. [7] outlined the two amphidromes in the north-west and south-east of New Zealand. Therefore the wave is trapped because of these forced waves that act on both coasts. Then the wave pattern is not determined by only resonance characteristics but must take into consideration more complex physics.

We will next compare the elevation amplitude and phase of *Gerris* solution with observations. The results
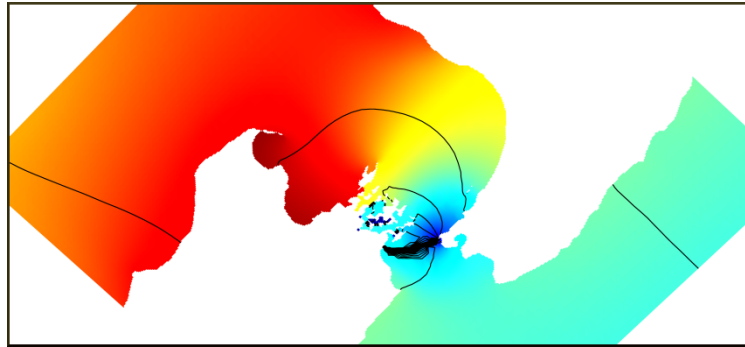

Figure 18: Amphidromic point in Cook Strait. Amplitude is shaded using decreasing colours : min = 0 cm max = 137 cm. Phase is drawn as lines : min = 0º   max = 360º.

obtained are provided in table 4. The maximum difference between observations and model results for the coastal sites presented here is 12.4 cm in amplitude and 16.3º in phase. Moreover, the observations data are not all the same quality. These results are summarised in Fig 19 and 20. Here *Gerris* solution of amplitude and phase is plotted against observation values. If the concordance was exact all the points would be on the line of unit gradient. Despite a perfect agreement, we notice that the error remains under 15 % for the amplitude and the difference is under 20º for the phase, which is a good agreement.

Location	Predicted elevation amplitude (cm)	Observed elevation amplitude (cm)	Predicted elevation phase (deg)	Observed elevation phase (deg)
Kapiti Is.	58.3	54.8	295.7	280.1
Little Kaiteriteri	133.2	130.9	290.5	275.9
Wellington	48.1	49.3	144.0	138.8
Riversdale	63.4	56.6	153.3	147.4
Nelson	134.3	129.8	289.5	280.3
Kaikoura	66.4	67.0	141.6	133.2
Charleston	119.0	105.7	324.0	307.6

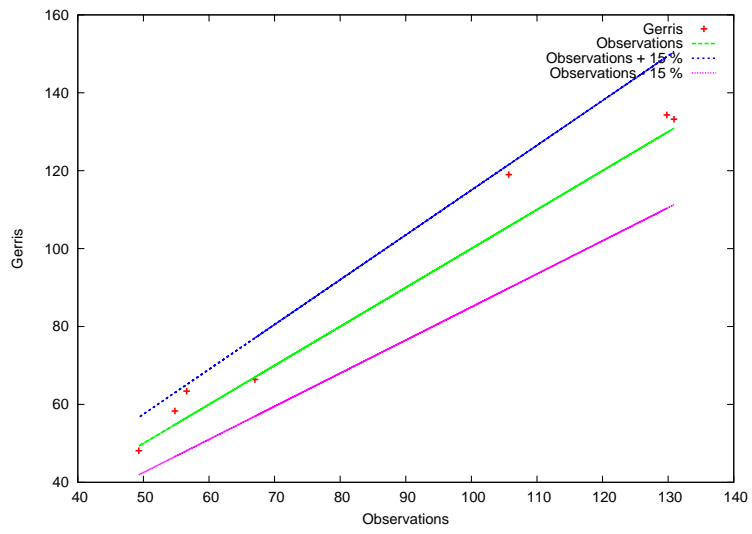Table 4: Comparison between predicted tidal elevation and observations.

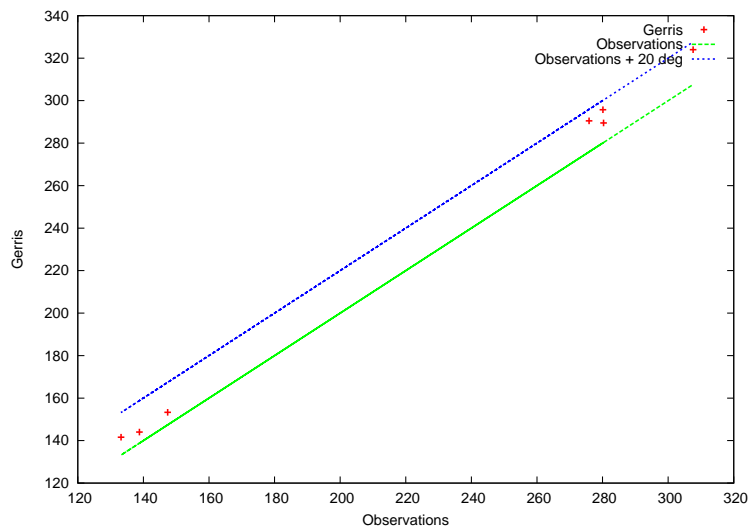Figure 19: Comparison of tidal elevation amplitude with observations.

Figure 20: Comparison of tidal elevation phase with observations.

3.8 Tidal circulation in Cook Strait

In this section we will analyse the tidal results obtained for the distribution of current.

Fig 21 displays the amplitude of u component of velocity corresponding to the M_2 tidal constituent. The solution referring to the driving model is shown on the left while *Gerris* solution is given on the right. We notice the good agreement between both models. Here the maximum amplitude coloured in red is 1 m/s and is registered in Cook Strait. Fig 22 provides a quantum of the error between the driving model and *Gerris*. The maximum contrasts occur in Cook Strait when we go closer to the coast, in very shallow water, but they are only 0.1 m/s which is quite satisfactory.
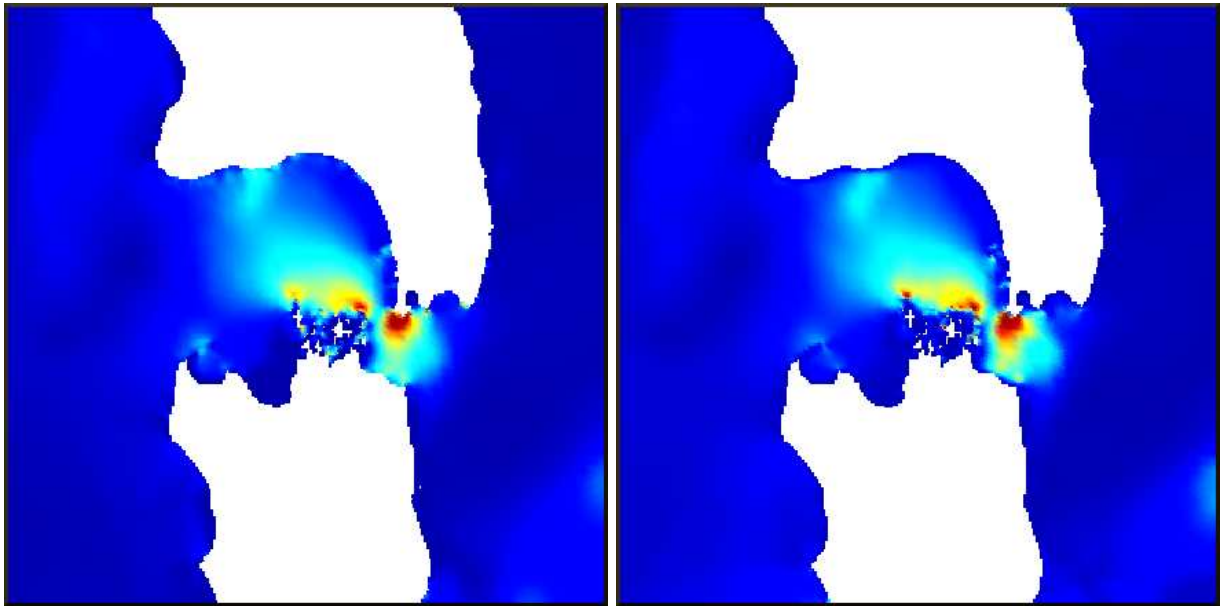
Figure 21: Amplitude of u component of velocity corresponding to the M_2 tidal constituent. Comparison between the driving model (on the left) and Gerris (on the right). Amplitude is shaded using decreasing colours : min = 0 m/s   max = 1 m/s.
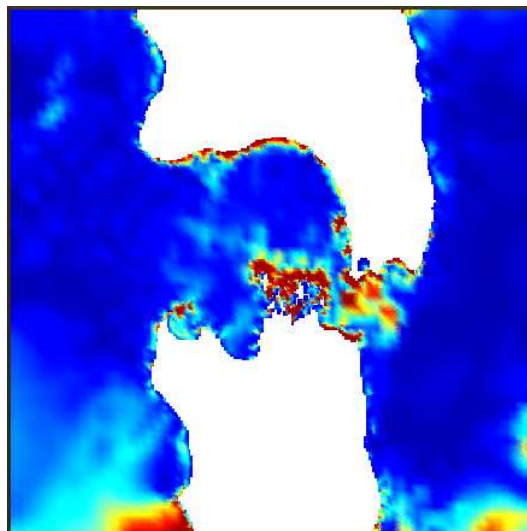

Figure 22: Amplitude error of u component of velocity. Error is shaded using decreasing colours : min = 0 m/s max = 0.1 m/s.

Fig 23 displays the amplitude of v component of velocity corresponding to the M_2 tidal constituent. As previously, the solution on the left refers to the driving model and the one on the right refers to *Gerris*. The

same conclusions apply here. There is a strong amplification of amplitude across Cook Strait with a maximum amplitude of 1 m/s. The amplitude error of v component of velocity is shaded on Fig 24. The major discrepancies of 0.1 m/s are shown in red and occur in Cook Strait where the topography is complex, and near Charleston and Kaikoura.
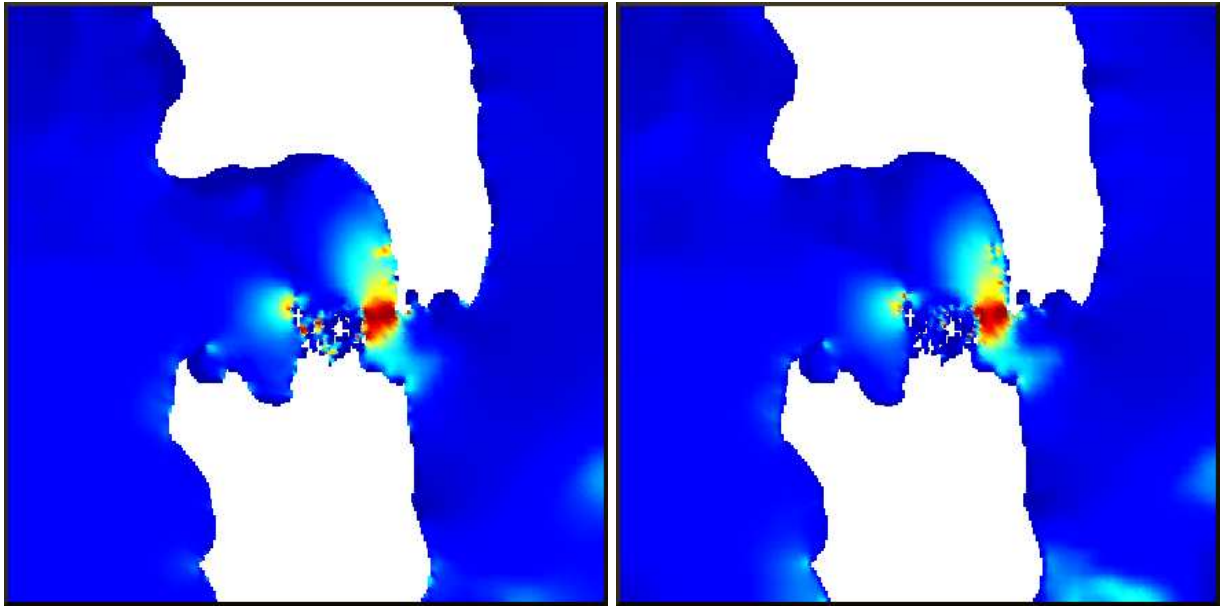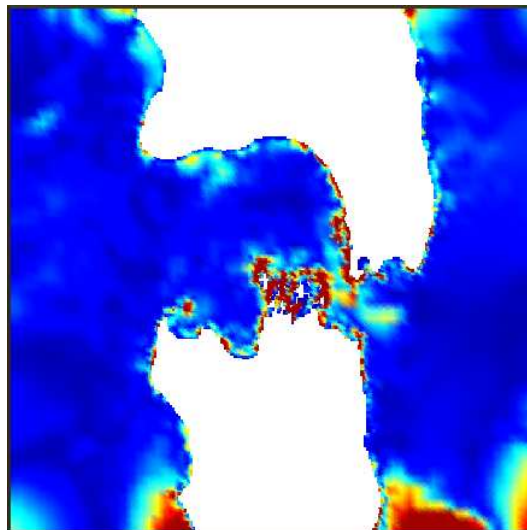

Figure 23: Amplitude of v component of velocity corresponding to the M_2 tidal constituent. Comparison between the driving model (on the left) and Gerris (on the right). Amplitude is shaded using decreasing colours : min = 0 m/s   max = 1 m/s.

Figure 24: Amplitude error of v component of velocity. Error is shaded using decreasing colours : min = 0 m/s max = 0.1 m/s.

Both component of velocity are well reproduced with small differences after comparing with the larger-scale model.

The velocity vector is shown on Fig.25. The tidal current vectors are displayed as arrows, indicating direction and velocity of the calculated tidal current at the given position and time. We notice the strongest currents across the strait as expected.

The tip of the velocity vector traces an ellipse as time progresses. We convert the north-going and east-going velocity components into ellipse parameters to be able to match the results. As defined in section 3.5 the velocity
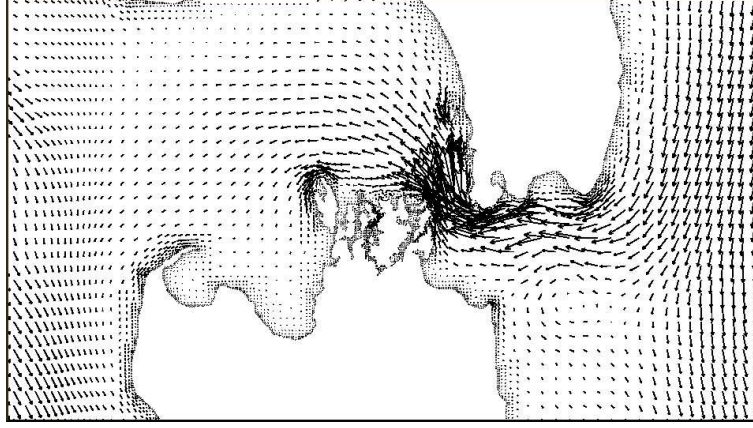
Figure 25: Instantaneous current vector. Scale = 100.

components can be expressed as tidal harmonics

$$u = M_u \cos\left(wt - \phi\right) = A \cos wt + B \sin wt, \tag{24}$$

$$v = M_v \cos\left(wt - \phi\right) = C \cos wt + D \sin wt, \tag{25}$$

where M_u and M_v are the amplitudes, ϕ is the phase, and w refers to the frequency. Then, A and C are the east and north cosine coefficients, while B and D are the east and north sine coefficients. We define the complex velocity $\tilde{V} = u + iv$ expressed in terms of counter-clockwise U^+, and clockwise, U^{-*}, complex amplitudes as

$$\tilde{V} = U^+ \exp\left(iwt\right) + U^{-^*} \exp\left(-iwt\right), \tag{26}$$

where the asterisk indicates the complex conjugate. The complex amplitudes can be written $U^+ = A^+ \exp\left(i\phi^+\right)$ and $U^- = A^- \exp\left(i\phi^-\right)$, where $A^\pm$ and $\phi^\pm$ represent real counter-clockwise $(+)$ and clockwise $(-)$ amplitudes and phases. Then tidal current ellipse attributes can be represented by three parameters: the semi-major axis or maximum current velocity a (positive quantity), the semi-minor axis b, and the inclination or the angle that the semi-major axis makes with east, θ, measured counter-clockwise. In terms of the above quantities, the ellipse parameters can be written

$$a = A^+ + A^-, \tag{27}$$

$$b = A^+ - A^-, \tag{28}$$

$$\theta = \frac{(\phi^+ + \phi^-)}{2}. \tag{29}$$

A forth parameter, the eccentricity, is defined as

$$e = \frac{a^2 - b^2}{a^2}. \tag{30}$$

For each tidal constituent, the current vector rotates around the ellipse. The direction of rotation is indicating by attaching a sign to the eccentricity. By convention, positive eccentricity is anticlockwise rotation of the current vector around the tidal ellipse.

Fig 26 provides a comparison in Cook Strait between tidal ellipses given by *Gerris*, displayed in red, and the ellipses corresponding to the driving model, displayed in black. Despite slight differences, the ellipses stack quite well.

Furthermore, to make a validation of the distribution of current, we need to compare our results to other data. Stanton et al. [1] have analysed the tidal currents using the high-resolution encompassing model developed by Walters et al. [14]. However, as shown on the map, Fig 27, the lack of observed data in the geographical region of interest did not allow us to make many comparisons. In fact, practically, it is not easy to obtain accurate current measurements. NIWA and its predecessor organisations have been deploying recording current meters since 1970. These data are archived at NIWA, but the database covering the concerning region around Cook Strait area is reduced. Fig 28 provides a comparison between both model (driving-model and *Gerris*) and measurements, for the available sites shown on Fig 27. For a better legibility, we have plotted on Fig 29–35 the ellipses for each site in order to discuss the results and their accuracy.
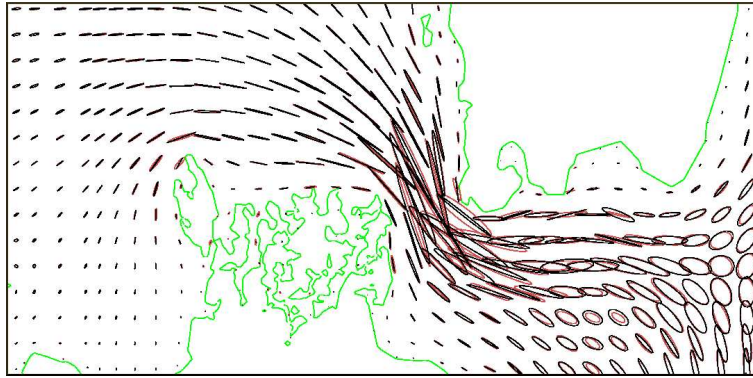
Figure 26: Tidal ellipses in Cook Strait. Instantaneous values. Scale = 35.
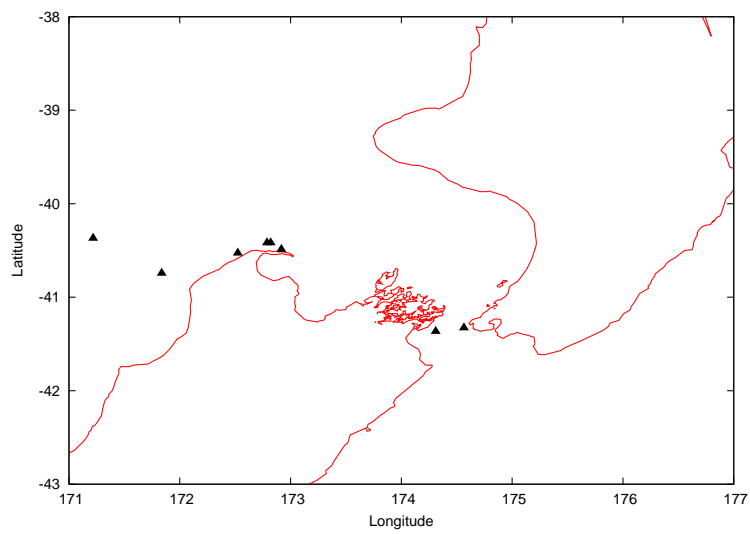

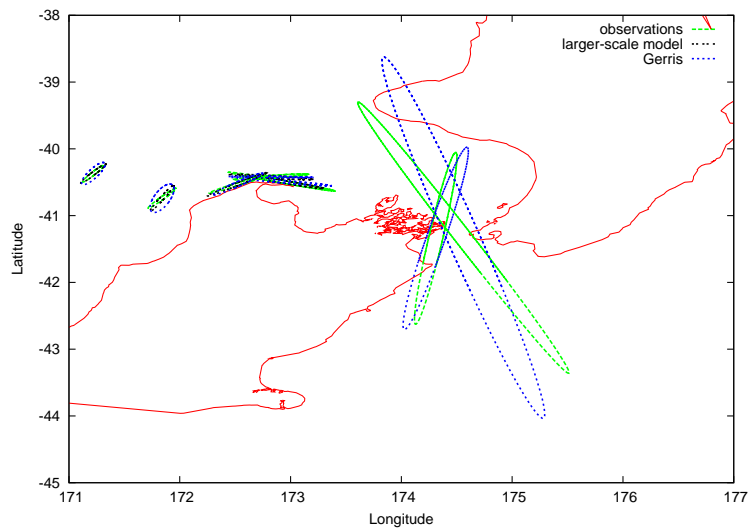Figure 27: Points from which computed results are compared with observations.

Figure 28: Comparison of Gerris tidal ellipses with the larger-scale model and observations. 1º longitude = 50 cm/s.
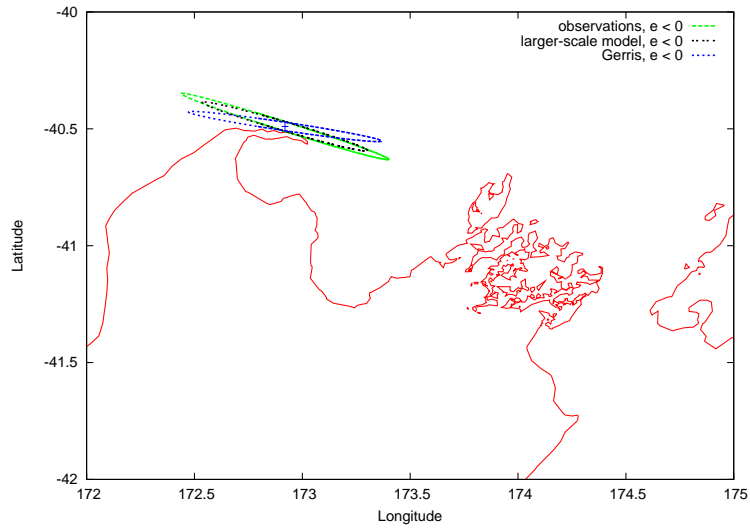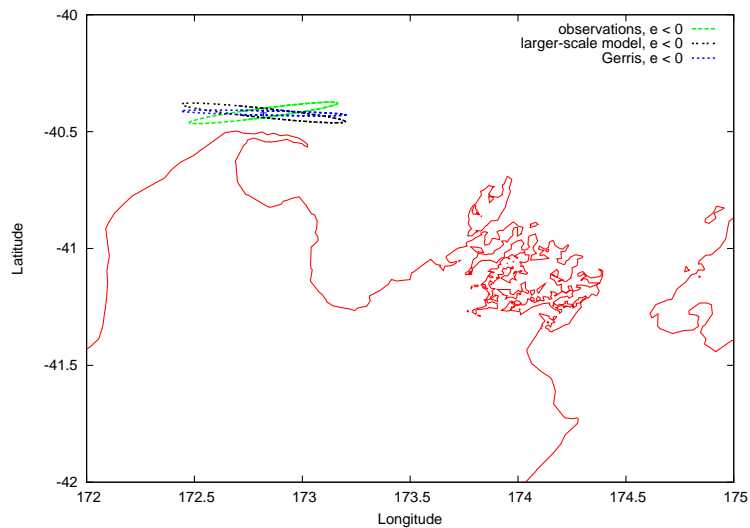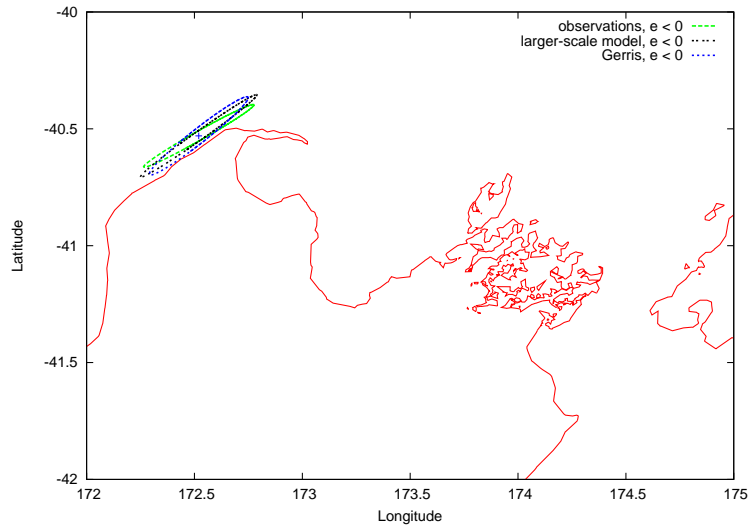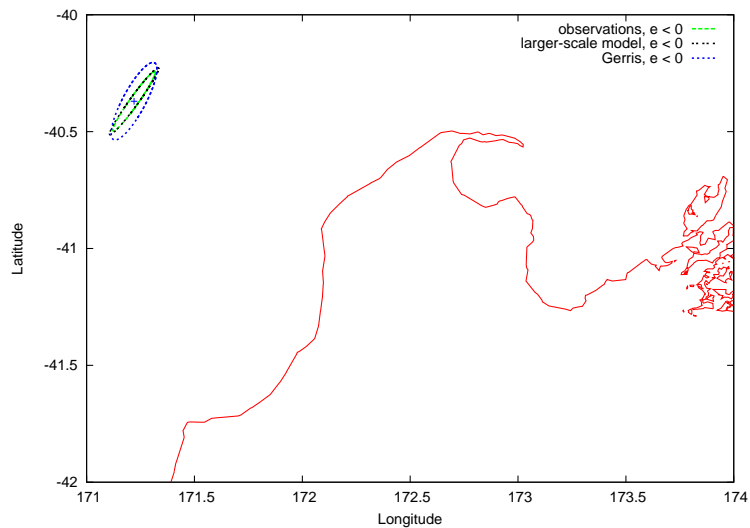
Figure 29: Comparison of tidal ellipses predicted by *Gerris*, with the larger-scale model and observations, for a point located at 172.9167 E 40.4883 S. Concerning the measurements the water depth is 41 m and the instrument depth is 21 m. 1° longitude = 50 cm/s.
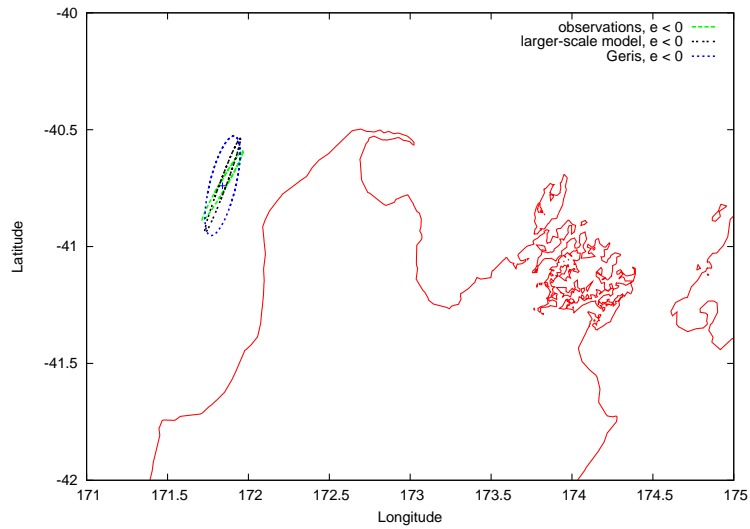

Figure 30: Comparison of tidal ellipses predicted by *Gerris*, with the larger-scale model and observations, for a point located at 172.7867 E 40.4183 S. Concerning the measurements the water depth is 78 m and the instrument depth is 23 m. 1° longitude = 50 cm/s.

Figure 31: Comparison of tidal ellipses predicted by *Gerris*, with the larger-scale model and observations, for a point located at 172.5233 E 40.5283 S. Concerning the measurements the water depth is 78 m and the instrument depth is 38 m. 1° longitude = 50 cm/s.

Figure 32: Comparison of tidal ellipses predicted by *Gerris*, with the larger-scale model and observations, for a point located at 171.2183 E 40.3700 S. Concerning the measurements the water depth is 550 m and the instrument depth is 100 m. 1° longitude = 50 cm/s.

Figure 33: Comparison of tidal ellipses predicted by *Gerris*, with the larger-scale model and observations, for a point located at 171.8367 E 40.7433 S. Concerning the measurements the water depth is 140 m and the instrument depth is 70 m. 1° longitude = 50 cm/s.
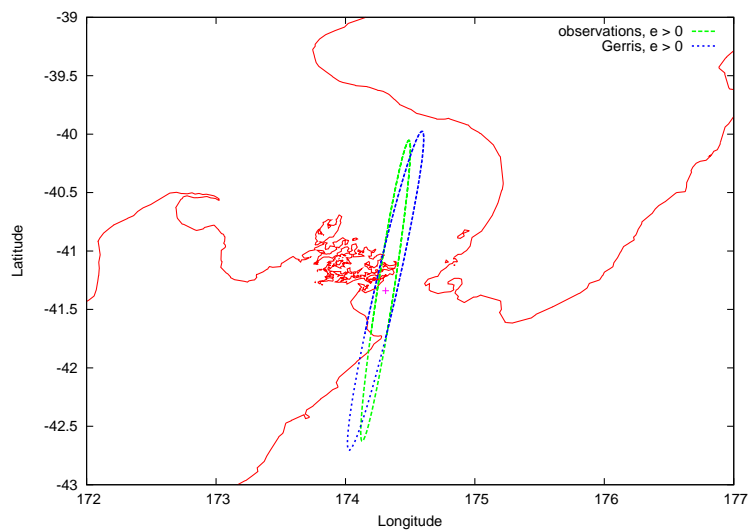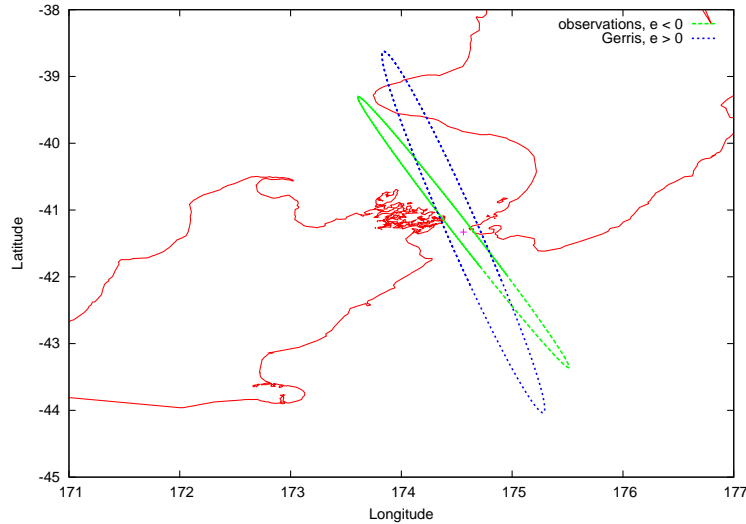

Figure 34: Comparison of tidal ellipses predicted by *Gerris*, with the larger-scale model and observations, for a point located at 174.31 E 41.366 S. Concerning the measurements the instrument depth is 50 m. 1° longitude = 50 cm/s.

Figure 35: Comparison of tidal ellipses predicted by *Gerris*, with the larger-scale model and observations, for a point located at 174.565 E 41.328 S. Concerning the measurements the instrument depth is 50 m. 1° longitude = 50 cm/s.

The results differ from on site to another. Commonly, the agreement is quite good between both model and observations even if the solution given by the larger-scale model is more in concordance with measurements than *Gerris* is. There are some discrepancies in the ellipse orientation as shown on Fig 29, 30 and 35. The predicted ellipses in Cook Strait (Fig 34 and Fig 35) are quite accurate in spite of the difficulty to reproduce the behaviour of current in this area. Besides, in Fig 29–35, e refers to the eccentricity and allows us to check the rotation sense of the current vector for each solution. In Fig.34, the sign of the eccentricity is not in agreement with the other results which means that at this point, the predicted current vector rotates in the wrong direction while describing the tidal ellipse.

In this section, we have compared the distribution of current with available measurements and with the driving-model. However, the larger-scale model and *Gerris* are not based on the same physical assumptions. Indeed, in *Gerris*, we adopted a linear law for friction whereas Walters et al. [14] adopted a quadratic law. Moreover, our model is absolutely linear as we did not take into account advection terms in the momentum equations and also because we defined the equation of mass conservation as a function of H_0 the depth in absence of motion, and not as a function of the total depth H. The larger-scale model is based on shallow water equations too, but some non-linear terms were retained. These differences may have an influence on the resulting solution, particularly on the distribution of current, and could explain some of the disparities obtained. Furthermore, the lack of observed data did not allow us to make accurate comparisons. Then, for the points where the gap between observations and the global scale model was too large, it was difficult to claim which data were the most accurate. Finally, the measurements were not reliable for all the sites. In fact, for each location we had several measurements referring to different instrument depths. We only took into consideration the deeper observations to adequately reproduce currents. However, the best thing would be to get measurements of the vertically averaged velocity. This would integrate the horizontal velocity over the full depth of the ocean and therefore it would provide a reliable measure of current variability.

Therefore, taking into account these remarks, we consider the distribution of current given by *Gerris* to be satisfactory.

4   Conclusion

In this report, we have examined the accuracy of the tidal response of a 500 km wide area around Cook Strait. We only took into consideration the lunar semi-diurnal constituent M_2. The distribution of amplitude and phase was calculated using a numerical model based on the linearized 2-dimensional shallow water equations, and driven by Walters et. al [14] larger-scale encompassing model data.

We have run a set of simulations using *Gerris* to validate the model. First, we compared the solution given by *Gerris* with the larger-scale model solution for different open-boundary conditions, in order to choose the best input. Flather iterative condition appeared to give more accurate results than the classical non-iterative

approach. That is why the model was driven using this radiation condition.

Then the resulting solution was compared with the encompassing model solution and with observations. Our aim was to acquire a solution as accurate as the driving-model results. The physical pattern of tides was well reproduced and the tidal range obtained was realistic. The M_2 tidal solution obtained for sea elevation was in very good agreement with the driving model and in quite good agreement with observations. Moreover, despite some discrepancies and taking into consideration the difficulty to reproduce the distribution of current and to make accurate comparisons, the tidal currents obtained were also in good agreement with the driving model and with measurements. Therefore we meet the requirements and consider our objective reached.

However, the present results indicate that it would be worthwhile to investigate the performance of the model by improving the bathymetry. In fact, the bathymetry used in *Gerris* (see Fig 1) was extracted from the larger-scale model. Thus, smaller scale regions are not well resolved in our model. Consequently, to improve our results we could run another set of simulations and focus on a small area where the bathymetry would be refined , in order to check the accuracy of the solution near the bays.

Finally, it would be profitable to refine the spatial resolution of the discretisation, particularly near solid boundaries, to take into consideration the complexity of the topography. This may improve significantly the description of the dynamics in Cook Strait and will allow us to confirm the validation of the numerical model.

# Appendix A   Major harmonic components contributing to the astronomical tides

| Symbol	Period	Frequency $(10^{-4}$rad/s$)$	Description
M_2	12h25	1.40563	Principal lunar, semi-diurnal
S_2	12h00	1.45444	Principal solar, semi-diurnal
N_2	12h40	1.37880	Larger lunar elliptic, semi-diurnal
K_2	11h58	1.45837	Lunar-solar declinational, semi-diurnal
O_1	25h49	0.67596	Principal lunar, diurnal
K_1	23h56	0.72921	Lunar-solar declinational, diurnal
P_1	24h04	0.72516	Principal solar, diurnal
Q_1	26h52	0.64953	Larger lunar elliptic, diurnal

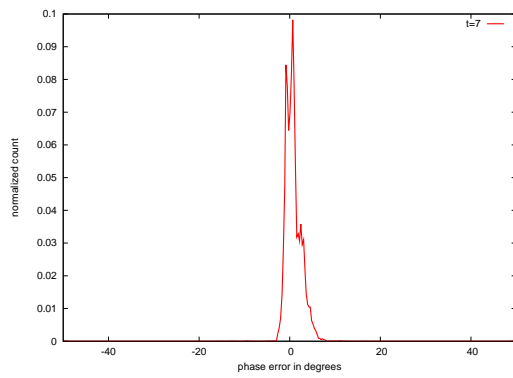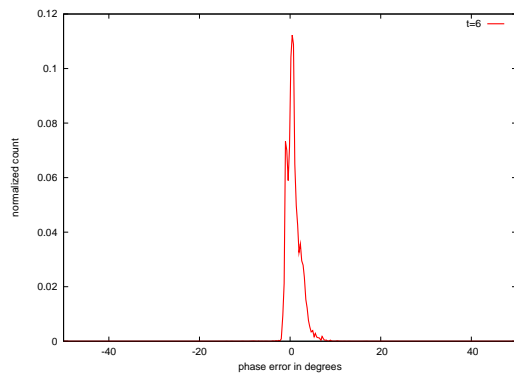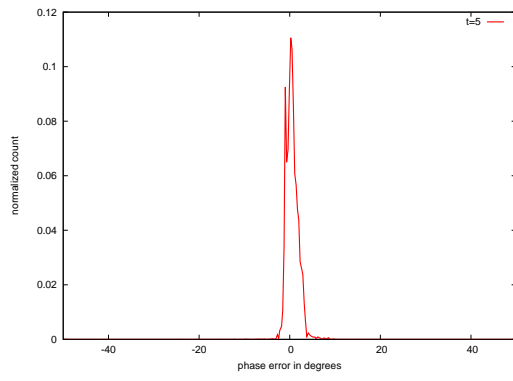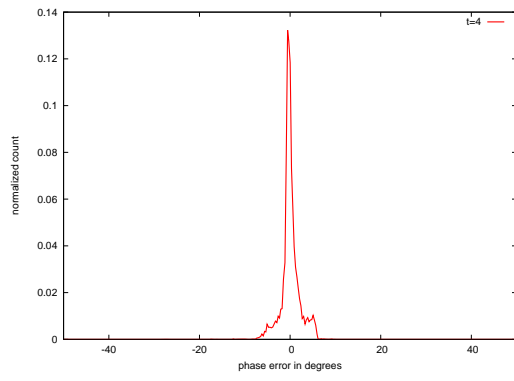Table 5: List of major tidal constituents.

Appendix B   Illustration of the convergence of the solution using Flather iterative condition
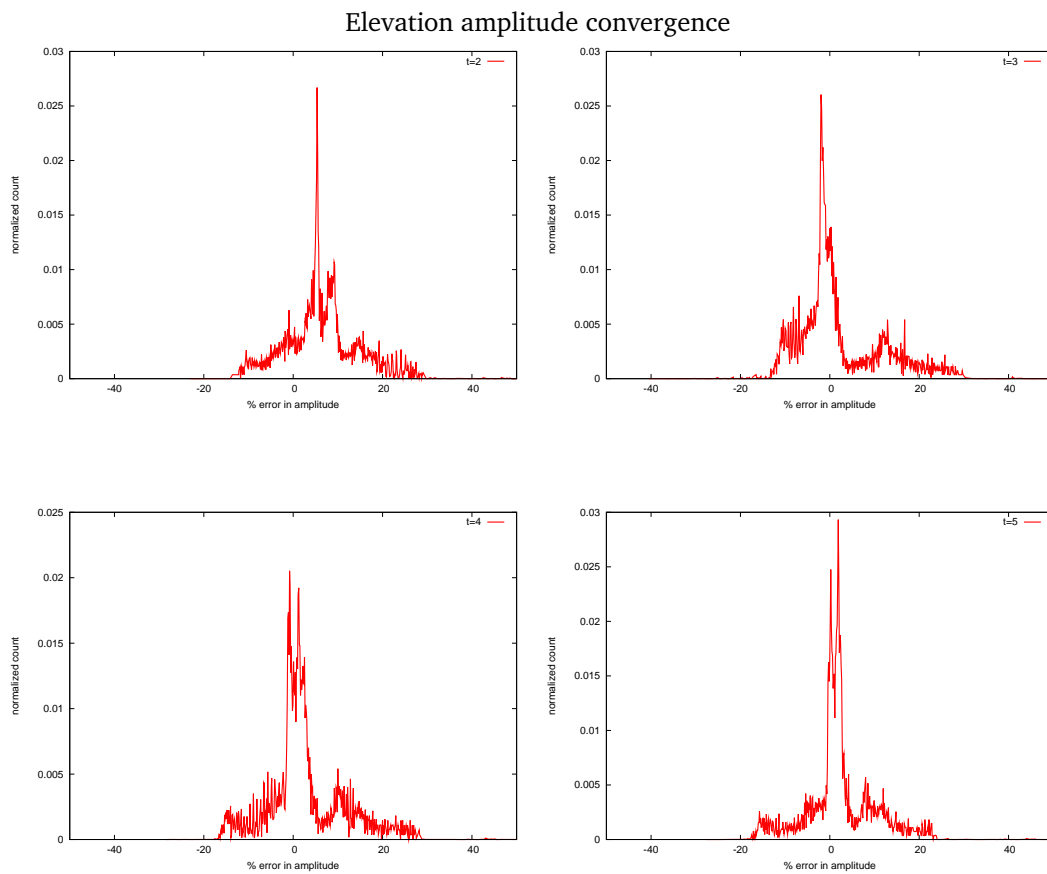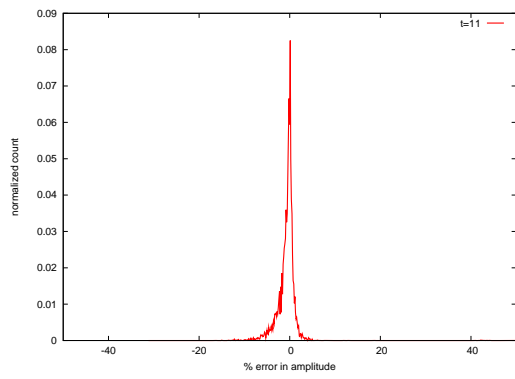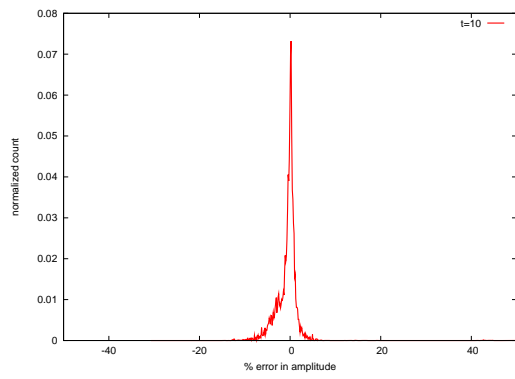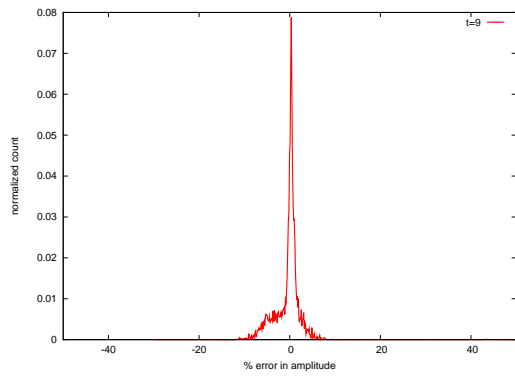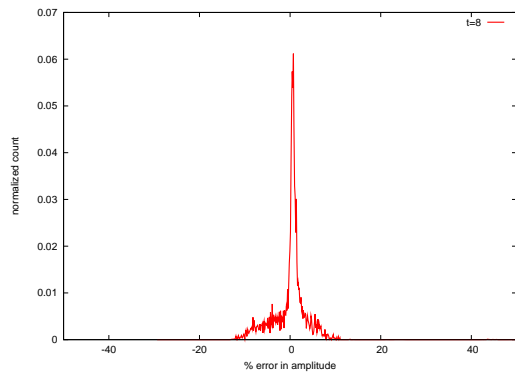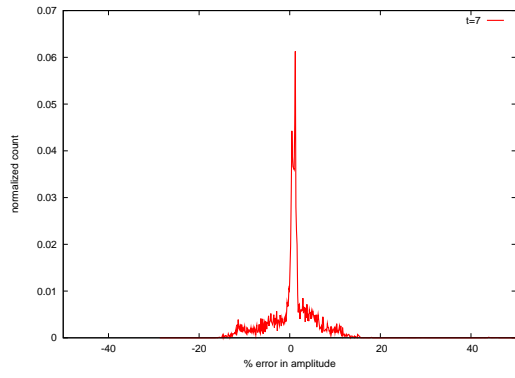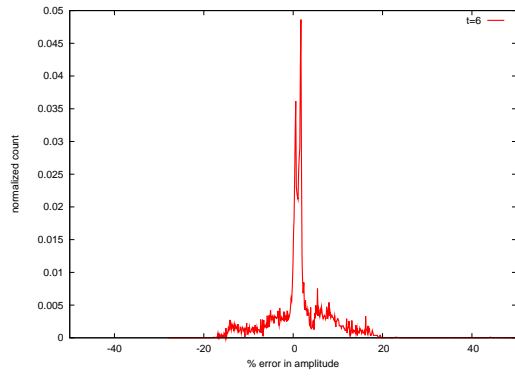
Elevation phase convergence
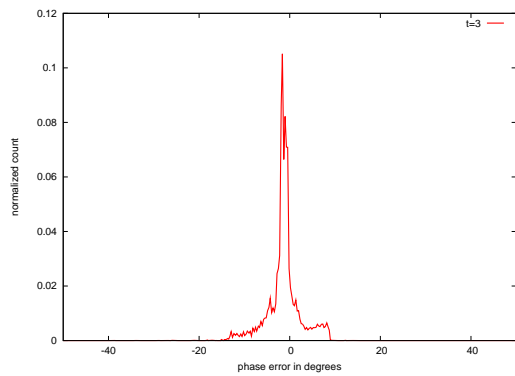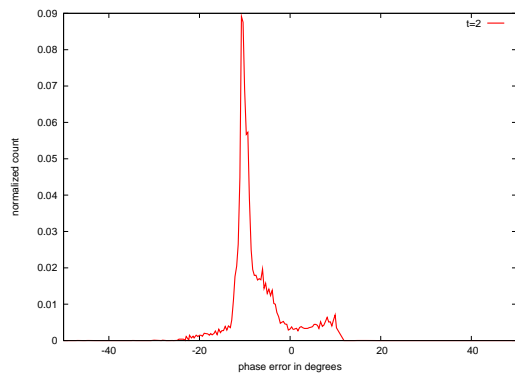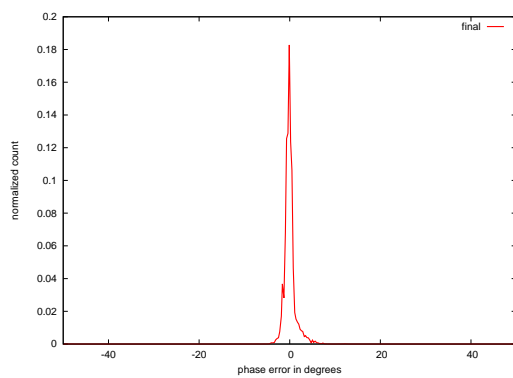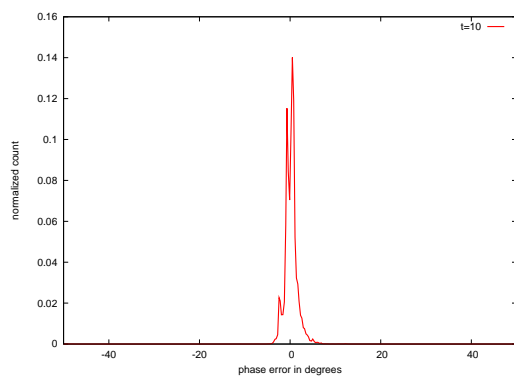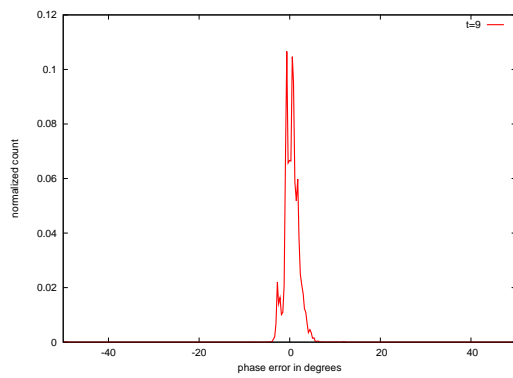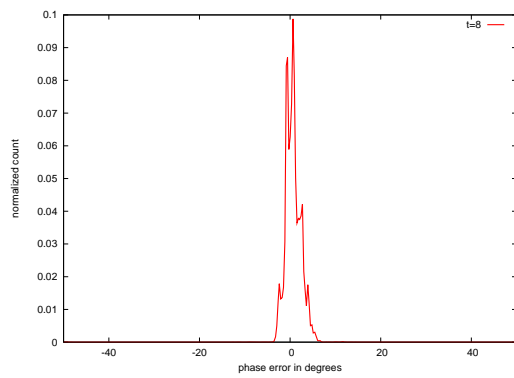
Appendix C   NIWA:*"where the waters meet the sky "*

NIWA's mission is to provide a scientific basis for the sustainable management and development of New Zealand's atmospheric, marine and freshwater systems and associated resources. Established in 1992 as one of nine New Zealand Crown Research Institutes (CRIs), NIWA operates as a stand-alone company with its own board of directors and its shares held by the Crown.

The company has a staff of around 630, annual revenue of 84 million derived from competition-based research grants and commercial enterprise, and assets of 65 million. The different consultancy services help clients solve problems on the use and management of: Atmosphere and Climate, Coast and Oceans, Freshwater, Fisheries and Aquaculture.

Spread throughout New Zealand, NIWA has its corporate headquarters in Auckland, main research campuses in Auckland, Hamilton, Wellington, Nelson, Christchurch and Lauder, and field offices in the smaller centres. Research vessels are maintained in Hamilton, Wellington and Christchurch. The company has subsidiaries in Australia and the USA and a vessel company.

The majority of NIWA's research funding comes from the Public Good Science and Technology fund, administered by the Foundation for Research, Science and Technology, and from the Ministry of Fisheries. NIWA staff also participate widely in international initiatives, representing New Zealand in such fora as the Intergovernmental Panel on Climate Change (IPCC)and the United Nations Environment Programme (UNEP).

Moreover, NIWA is a technology-driven, innovative company in the business of creating wealth as well as providing policy advice. Its clients include New Zealand and overseas governments; local and regional councils; industries such as energy, fisheries, forestry, dairy, horticulture, and agriculture; port authorities and oil companies; consulting engineers; and others who use water and air for commercial and recreational purposes.

NIWA's Maori name *Taihoro Nukurangi* describes its activity as studying the waterways and the interface between the earth and the sky. Actually, *Taihoro* is the flow and movement of water (from *tai* for "coast ", "tide "and *horo* for "fast moving "). Nukurangi is the interface between the sea and the sky (i.e., the atmosphere). Together, *Taihoro Nukurangi* mean "where the waters meet the sky ".

References

[1] Derek G. Goring Basil R. Stanton and Rob G. Bell. Observed and modelled tidal currents in the New Zealand region. *New Zealand Journal of Marine and Freshwater Research*, 35:397–415, 2001.

[2] J.A.T. Bye and R.A. Heath. The New Zealand semi-diurnal tide. *Journal of Marine Research*, 33:423–442, 1975.

[3] F. Lyard P. Vincent C. LeProvost, M.L. Genco and P. Canceil. Spectroscopy of the world ocean tides from a finite-element hydrodynamic model. *Journal of Geophysical Research*, 99:24777–24797, 1994.

[4] L. Debreu E.Blayo. Revisiting open boundary conditions from the point of view of characteristic variables. *Preprint submitted to Elsevier Science*, 19 april 2004.

[5] R.A. Flather. A tidal model of the north-west European continental shelf. *Mémoires de la Société Royale des Sciences de Liège*, 6:141–164, 1976.

[6] R.A. Flather and N.S. Heaps. Tidal computations for morecambe bay. *Geophys. J.R. astr. Soc.*, 42:489–517, 1975.

[7] M.G.G. Foreman G.D. Egbert, A.F. Bennett. Topex/poseidon tides estimated using a global inverse model. *Journal of Geophysical Research*, 99:24821–24852, 1994.

[8] R.A. Heath. Review of the physical oceanography of the seas around New Zealand–1982. *New Zealand Journal of Marine and Freshwater Research*, 19:79–124, 1985.

[9] J. Nycander and K. Ds. Open boundary conditions for barotropic waves. *Journal of Geophysical Research*, 108, 2003.

[10] A. Shchepetkin P. Marchesiello, J.C. McWilliams. Open boundary conditions for long-term integration of regional oceanic models. *Ocean Modelling*, 3:1–20, 2001.

[11] E.D. Palma and R.P. Matano. On the implementation of passive open boundary conditions for a general circulation model: the barotropic mode. *Journal of Geophysical Research*, 103:1319–1341, 1998.

[12] Joseph Pedlosky. *Geophysical Fluid dynamics*. Springer-Verlag, New York, second edition, 1987.

[13] L.P. Roed and C.K. Cooper. Open boundary conditions in numerical ocean models. *Advanced Physical Oceanographic Numerical Modelling*, 1986.

[14] Derek G. Goring Roy A. Walter and Rob G. Bell. Ocean tides around New Zealand. *New Zealand Journal of Marine and Freshwater Research*, 35:567–579, 2001.